PHYSICAL REVIEW B **108**, 024420 (2023)

Anomalous Nernst effect in Mn_3NiN thin films

Sebastian Beckert,[1] João Godinho,[2,3] Freya Johnson,[4] Jozef Kimák,[3] Eva Schmoranzerová,[3] Jan Zemen,[5]
Zbyněk Šobáň,[2] Kamil Olejník,[2] Jakub Železný,[2] Joerg Wunderlich,[6] Petr Němec,[3] Dominik Kriegner,[1,2]
Andy Thomas,[1,7] Sebastian T. B. Goennenwein,[8] Lesley F. Cohen,[4] and Helena Reichlová[1,2]
[1] *Institut für Festkörper- und Materialphysik, Technische Universität Dresden, 01062 Dresden, Germany*
[2] *Institute of Physics ASCR, v.v.i., Cukrovarnická 10, 162 53 Prague, Czech Republic*
[3] *Faculty of Mathematics and Physics, Charles University, Ke Karlovu 3, 121 16 Prague, Czech Republic*
[4] *Department of Physics, Blackett Laboratory, Imperial College London, London SW7 2AZ, United Kingdom*
[5] *Faculty of Electrical Engineering, Czech Technical University in Prague, Technická 2, 166 27 Prague, Czech Republic*
[6] *Institute of Experimental and Applied Physics, University of Regensburg, Universitätsstraße 31, 93051 Regensburg, Germany*
[7] *Leibniz Institute of Solid State and Materials Science (IFW Dresden), Helmholtzstrasse 20, 01069 Dresden, Germany*
[8] *Department of Physics, University of Konstanz, 78457 Konstanz, Germany*

(Received 5 December 2022; revised 21 April 2023; accepted 14 June 2023; published 20 July 2023)

The observation of a sizable anomalous Hall effect in magnetic materials with vanishing magnetization has renewed interest in understanding and engineering this phenomenon. Antiferromagnetic antiperovskites are one of the emerging material classes that exhibit a variety of interesting properties owing to a complex electronic band structure and magnetic ordering. Reports on the anomalous Nernst effect and its magnitude in this class of materials are, however, very limited. This scarcity may be partly due to the experimental difficulty of reliably quantifying the anomalous Nernst coefficient. Here, we report experiments on the anomalous Nernst effect in antiferromagnetic antiperovskite Mn_3NiN thin films. Measurement of both the anomalous Hall and Nernst effects using the same sample and measurement geometry makes it possible to directly compare these two effects and quantify the anomalous Nernst coefficient and conductivity in Mn_3NiN. We carefully evaluate the spatial distribution of the thermal gradient in the sample and use finite-element modeling to corroborate our experimental results.

DOI: 10.1103/PhysRevB.108.024420

I. INTRODUCTION

In magnetically ordered materials, a thermal gradient can induce a voltage perpendicular to both the thermal gradient direction and the magnetic order vector. This thermally generated transverse voltage is referred to as the anomalous Nernst effect (ANE) and can be understood as a thermal counterpart of the anomalous Hall effect (AHE). In recent years, the ANE has attracted increasing attention because, similar to the AHE, the various underlying mechanisms have been disentangled [1]. A key step was the development of the Berry phase concept, which links the intrinsic AHE and ANE to the integration of the Berry curvature over the first Brillouin zone [2]. When the combined time reversal and inversion symmetry and combined time reversal and translation symmetry operations are broken and the corresponding integral is nonzero, intrinsic contributions to the ANE and AHE can exist. However, the breaking of these combined symmetries does not imply that the spins are ferromagnetically ordered. As a consequence, the ANE was observed in materials that were previously thought not to allow this phenomenon because of a vanishing net magnetization [3]. Recent progress also showed a path to increase the ANE response, leading to the observation of very large ANE coefficients in emerging materials such as Fe_3Sn, $UCo_{0.8}Ru_{0.2}Al$, and $YbMnBi_2$ [4–6] by engineering the electronic band structure and the position of the Fermi level.

Despite the major advances that have been made in recent years, the ANE is not yet fully understood. The field dependence of the ANE in comparison to that of the AHE and the expected anisotropy in nontrivial materials are still topics under active discussion [7]. The ANE is dominated by the states in the proximity of the Fermi level. Therefore, in materials with a complex band structure the ANE can serve as a more sensitive probe of changes of the Fermi energy E_F than the AHE, which is proportional to the integral of the Berry curvature over all occupied states [8,9]. Another advantage of the ANE is related to the versatility of the thermal gradient. In thin antiferromagnetic films, the crystal and spin orientation are typically determined by epitaxial constraints and cannot be easily modified; therefore, measuring the AHE along different crystal directions can be challenging. In particular, measuring the AHE response for a current perpendicular to the thin-film plane requires tedious lithography and three-dimensional microfabrication [10]. By contrast, applying an out-of-plane thermal gradient using a focused laser beam is comparatively simple [11–13]. However, quantifying the thermal gradient in this measurement geometry is very challenging. Over the last few years, the ANE has also been discussed in the context of applications such as heat flux sensors [14]. Here, again, the antiferromagnetic ANE would be beneficial owing to the absence of magnetic stray fields. Despite these benefits, the ANE is far less studied than the AHE because control and quantification of an applied thermal gradient are especially challenging and not as straightforward as applying and measuring an electric current, as used to determine the AHE.

The promising family of antiperovskite manganese nitrides Mn_3XN, where X represents Ni, Sn, or Ga, is actively studied [15–17]. These materials have been reported to exhibit the AHE [18–22] as a consequence of the symmetries broken by the noncollinear magnetic order and the resulting Berry curvature [7]. As described in more detail by Zhou *et al.* for Mn_3NiN [7], Chen *et al.* for Mn_3Ir (which has a noncollinear antiferromagnetic structure similar to that of Mn_3NiN) [2], and Gurung *et al.* for Mn_3GaN [16], the magnetic structure of the Γ^{4g} phase in combination with the spin-orbit coupling breaks the necessary symmetries (e.g., combined time reversal symmetry and translation symmetry as well as combined time reversal symmetry and inversion symmetry), which allows a nonvanishing anomalous Hall conductivity (AHC) and anomalous Nernst conductivity (ANC) in Mn_3NiN [2,7,23]. In contrast, in the Γ^{5g} phase a mirror symmetry is preserved, which results in a vanishing AHC and ANC [7]. Theoretical calculations show that the spin-orbit coupling is necessary for a nonvanishing AHC and ANC [18]. The AHE in Mn_3NiN was discussed in the context of Weyl crossings in the band structure [24]. We note that the existence of Berry curvature and the AHE or ANE is determined by symmetry and does not require the existence of Weyl points or any special topology. From our measurements we cannot make any clear conclusion about whether the Weyl points contribute to the AHE and ANE. It was shown by neutron diffraction that in epitaxial Mn_3NiN thin films the Γ^{4g} phase can be stable to lower temperatures than in the bulk material [25]. Interestingly, strain control of the AHE was demonstrated [25–28], which is an important step toward strain-controlled switching of the AHE response, as recently reported for Mn_3Sn [29]. At the same time, very limited reports on the ANE in manganese nitrides are available: the ANE was very recently reported in Mn_3SnN [30] while an out-of-plane thermal gradient was applied. A laser-induced thermal gradient was also used to visualize the magnetic structure of Mn_3NiN without quantifying the ANE [13]. Consequently, a systematic evaluation and quantification of the ANE and AHE in a single sample with a well-defined thermal gradient has yet to be performed.

In this paper, we report a systematic study of the anomalous Nernst effect in antiferromagnetic thin-film Mn_3NiN. In this study, the ANE is generated by an in-plane thermal gradient, with special attention paid to the spatial distribution of the thermal gradient, which we compare to numerical simulations based on the finite-element method (FEM) as implemented in COMSOL MULTIPHYSICS [31]. We measure an anomalous Nernst coefficient of $0.0382\,\mu V/K$ at temperatures between 150 and 190 K, which is comparable to the reported Nernst coefficient of the closely related Mn_3SnN [30]. We propose that Mn_3NiN is not only a fundamentally interesting compound but also an ideal model system because its noncollinear magnetic structure in the (111) plane enables the generation of an ANE by both in- and out-of-plane thermal gradients in (001)-oriented thin films [13,22]. Moreover, the position of the Fermi energy can be tuned by strain induced from various substrates [25].

II. SAMPLE FABRICATION

The Mn_3NiN film with a thickness of 50 nm used in this study was grown by pulsed laser deposition on a single-crystal (001)-oriented $SrTiO_3$ (STO) substrate at a temperature of 400 °C. The growth and structural properties of Mn_3NiN films grown on STO substrates are described in detail in [26]. The film has a [001] film normal and a Néel temperature of $T_N = 230\,K$ [13]. Magnetization loops measured at several temperatures are depicted in Fig. 1(a). After the removal of the diamagnetic background from the substrate, the magnetization loops are still dominated by an S-shaped magnetization, which we attribute to soft ferromagnetic impurities in the substrate. This soft magnetization is removed as described in Sec. S3 of the Supplemental Material [32] and reveals the intrinsic magnetization which we attribute to the thin film, which is consistent with other Mn_3NiN films on a STO substrate [25,26].

The film was patterned into Hall bars with a width of 45 µm and transversal contacts with a length of 1800 µm using electron beam lithography and a wet etching process with diluted ferric chloride. After the film was etched, 50 nm thick platinum heaters and thermometers were fabricated by Pt sputtering using a lift-off process. The same sample geometry was previously used to measure the ANE in ferromagnetic Co_2MnGa thin films [33]. A false-color microscopy image of the resulting device is shown in Fig. 1(b).

The sample layout with on-chip heaters and thermometers enables direct measurement and comparison of the AHE and ANE for the same device. Owing to the sample geometry, the in-plane temperature gradient generated by Joule heating of the platinum heater is considerably smaller than the out-of-plane thermal gradient generated by a platinum heater on top of the thin film, as measured by You *et al.* for Mn_3SnN [30]. Thus, we measured smaller Nernst voltages in this study. However, this geometry has the advantage of allowing the temperature to be directly measured at different positions in our sample for use in evaluating the local temperature gradients, Nernst conductivities, and Nernst coefficients with higher accuracy.

III. HALL MEASUREMENTS

Figure 1(c) shows the temperature-dependent longitudinal conductivity σ_{xx}, which suggests a semimetallic character of the material that is consistent with the results of previous studies. The anomalous Hall effect was measured by applying a magnetic field perpendicular to the sample plane [see the coordinate system depicted in Fig. 1(b)]. The Hall resistivity ρ_{yx} was calculated as

$$\rho_{yx} = \frac{V_y}{I_x} t, \tag{1}$$

where the transversal voltage is denoted V_y, the source current is denoted I_x, and the film thickness is denoted t. We used the Hall resistivity to calculate the Hall conductivity as

$$\sigma_{yx} = -\frac{\rho_{yx}}{\rho_{xx}^2 + \rho_{yx}^2}, \tag{2}$$

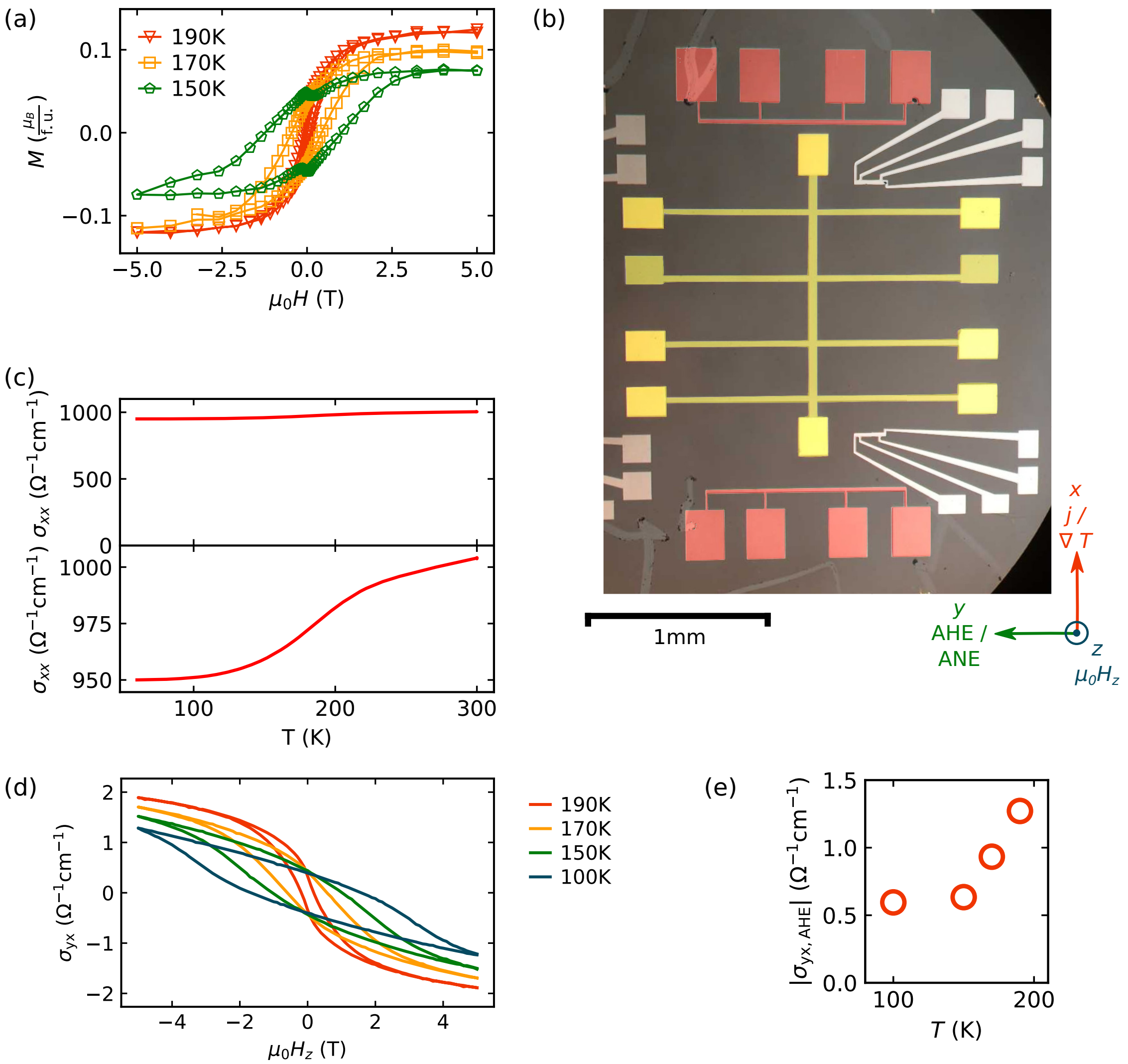

FIG. 1. Characterization of the $\mathrm{Mn_3NiN}$ films. (a) Magnetization loops measured with a magnetic field out of the sample plane at 190, 170, and 150 K after removing the ferromagnetic background. (b) False-color microscopy image of the $\mathrm{Mn_3NiN}$ Hall bar (yellow) with platinum heaters (red) and thermometers (white). (c) Temperature dependence of the longitudinal conductivity. (d) Magnetic-field dependence of the Hall conductivity at different temperatures. (e) Temperature dependence of the anomalous Hall conductivity.

where the longitudinal resistivity is denoted by ρ_{xx} [34]. The ordinary Hall contribution was subtracted via linear fitting to the Hall voltage at high fields to extract the anomalous contribution. The total Hall conductivity $\sigma_{yx} = \sigma_{yx,\mathrm{OHE}} + \sigma_{yx,\mathrm{AHE}}$ measured at various temperatures is shown in Fig. 1(d), and the temperature dependence of the anomalous Hall conductivity at saturated magnetization is shown in Fig. 1(e). Upon cooling, the anomalous Hall conductivity decreases, and the coercive field increases, in agreement with previous observations of $\mathrm{Mn_3NiN}$ films prepared on STO substrates and the magnetometry [18,35]. Assuming that the Mott relation is valid [34,36], the AHE provides an indication of the field dependence of the ANE signal. The data do not allow a clear separation of the extrinsic and intrinsic contributions. For further details we refer to Sec. S1 in the Supplemental Material [32] (see also Refs. [37–41] therein).

IV. NERNST MEASUREMENTS AND ANALYSIS OF TEMPERATURE GRADIENT

We measured the ANE by applying a current through the lithographically defined platinum heater stripe to generate a thermal gradient in the substrate via dissipation of the Joule heating, as schematized in Fig. 2(a). This scheme enabled us to heat one end of the sample with respect to the other end, resulting in the thermal gradient. We then used the lithographically defined thermometers to measure the temperature drop between the "cold" and "hot" ends of the device or, more generally, as a function of position on the surface (the spatial variation in the temperature gradient will be discussed later). We define the temperature gradient as $\nabla_x T = \frac{\Delta T}{d}$, where d is the distance between the two thermometers. We also measured the temperature as a function of position on the sample using two transversal arms of the Hall bar as resistive temperature sensors [see Fig. 2(a)], which resulted in a more local

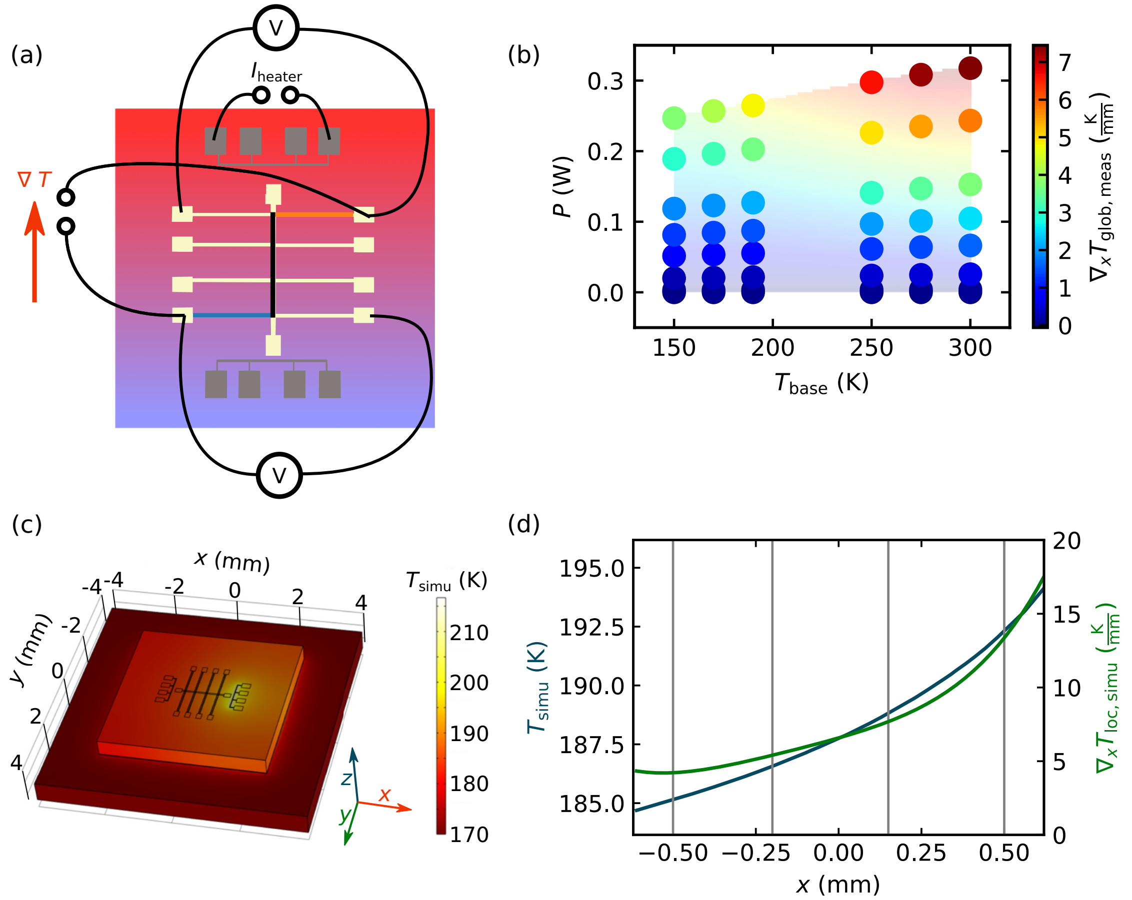

FIG. 2. Calibration of the local temperature gradients. (a) Schematic of the temperature gradient applied to the sample, with an example of the measurement geometry used to evaluate the global temperature gradient with the sample arms as resistive thermometers. The sections of the Hall bar arm highlighted in orange and blue denote the temperatures on the hot and cold sides of the bar, respectively. (b) Measured values of the thermal gradient (points) and the corresponding linear interpolation (colored area) as a function of the heater power and the sample base temperature T_{base}. (c) FEM simulated temperature profile over the sample for $T_{\text{base}} = 170$ K. (d) FEM simulated temperature profile and temperature gradients along the Hall bar for $T_{\text{base}} = 170$ K.

evaluation of the temperature gradient because we evaluated the temperature at the Hall bar and not at the position of the thermometers. We observed good agreement between the results for the two thermometry methods. The thermal gradient was experimentally measured at various base (cryostat) temperatures using various heater powers [Fig. 2(b)]. Note that we also performed the experiments using two different cryostats with various chip carriers, sample mountings, and helium pressures in the variable-temperature insert of the cryostats. Comparing the results obtained using the two setups, as well as the two thermometry methods, showed that the different experimental conditions result in differences in the thermal gradient on the order of only 20%. Therefore, the two experimental setups could be modeled by one set of parameters in our simulations. We present the results obtained using the various measurement setups and the corresponding thermometry below. The spatial variation in the thermal gradient depends strongly on the sample material parameters. We modeled the heat transfer in the device, including the substrate, glue, and chip carrier, using a realistic geometry and material-specific thermal conductivities. We employed the finite-element method to solve the model and determine the spatial dependence of the thermal gradient. The model includes the charge current through the heater, which provides Joule heating as an input to the thermal component. The conductivity of the thin platinum wire was obtained by fitting to the measured heater power of 0.26 W at a fixed base temperature of 170 K. The conductivity of 1 040 500 S/m is, as expected, lower than for bulk Pt. We used a thermal conductivity of 12 W/(Km) for the STO substrate [42]. As the STO substrate is glued to a ceramic chip carrier, which is clamped to a copper heat sink, a 0.2 mm thick layer with a thermal conductivity of 0.3 W/(Km) was added between the substrate and the chip carrier as thermal resistance of the glue in our simulations. A thermal conductivity of 0.37 W/(Km) was obtained for the 0.635 mm thick chip carrier by using this thermal conductivity as a fitting parameter. The temperature of the hottest transversal bar defined the fitting criterion. The simulation results show that the in-plane thermal gradient depends strongly on the thermal conductivity of the substrate, as well as on the thermal contact of the substrate with the heat sink. The values of the thermal conductivities and heat capacities used in the simulation are given in Table I. Figure 2(c) shows the simulated temperature profile for the sample surface.

TABLE I. Overview of the parameters used in the FEM simulations.

Material	Thermal conductivity W/(K m)	Heat capacity J/(K kg)
Mn_3NiN (film)	17	600
$SrTiO_3$ (substrate)	12	500
GE varnish (glue)	0.3	500
Al_2O_3 (chip carrier, fit parameter)	0.37	730
Pt (heater and thermometers)	71.6	133

In Fig. 2(d) we show the resulting temperature profile and gradient along the x direction at $y = 0\,\mathrm{mm}$ as blue and green curves, respectively. The resulting simulated difference in the temperatures averaged along the hottest and coldest transversal bars at a base temperature of 170 K and a heater power of 0.26 W is 5.88 K, whereas the measured global temperature difference is 4.16 K under the same conditions. As we use only the shape of the decay of the temperature gradient along y to rescale our measured temperature difference; this level of agreement is sufficient.

We determined the anomalous Nernst voltage at various pairs of transverse contacts to experimentally explore the spatial dependence of the applied temperature gradient $\nabla_x T$. The magnetic field was applied out of the sample plane [Fig. 3(d)]. The ANE signal was measured at base temperatures of T_{base} 150, 170, and 190 K. Subtracting the linear background corresponding to the ordinary Nernst contribution reveals a saturation of the Nernst signal. Figures 3(a)–3(c) show the measured anomalous Nernst voltages at different base temperatures T_{base} in comparison to the anomalous Hall conductivities discussed above. The coercive field of the ANE for each base temperature T_{base} is in agreement with the values measured based on the AHE. Note that the anomalous Nernst voltage plotted in Fig. 3 depends on the applied thermal gradient; therefore, one cannot directly compare the magnitude of the ANE. Thus, to perform such a comparison, we calculate the anomalous Nernst coefficient using the local temperature gradients at our transversal bars. This procedure is presented below.

To properly evaluate the ANE coefficient, it is essential to assess the spatial homogeneity of the signals. For this purpose, we recorded the ANE signal for different pairs of contacts, i.e., at different distances x from the heater. The data compiled in Figs. 4(a) and 4(b) show the field-dependent anomalous Nernst voltage for the transversal contact pair closest to and farthest from the heater, respectively. The ANE voltages measured on the two contact pairs differ by a factor of approximately 2.8, confirming the inhomogeneity of the temperature gradient expected from our FEM simulation, which predicts a factor of 2.5 between the local temperature gradients at these two contact pairs. We determined the anomalous Nernst coefficient S_{yx} using the following formula:

$$S_{yx} = \frac{V_y}{\nabla_x T_{\mathrm{loc,meas}} \times w_{\mathrm{bond}}}, \tag{3}$$

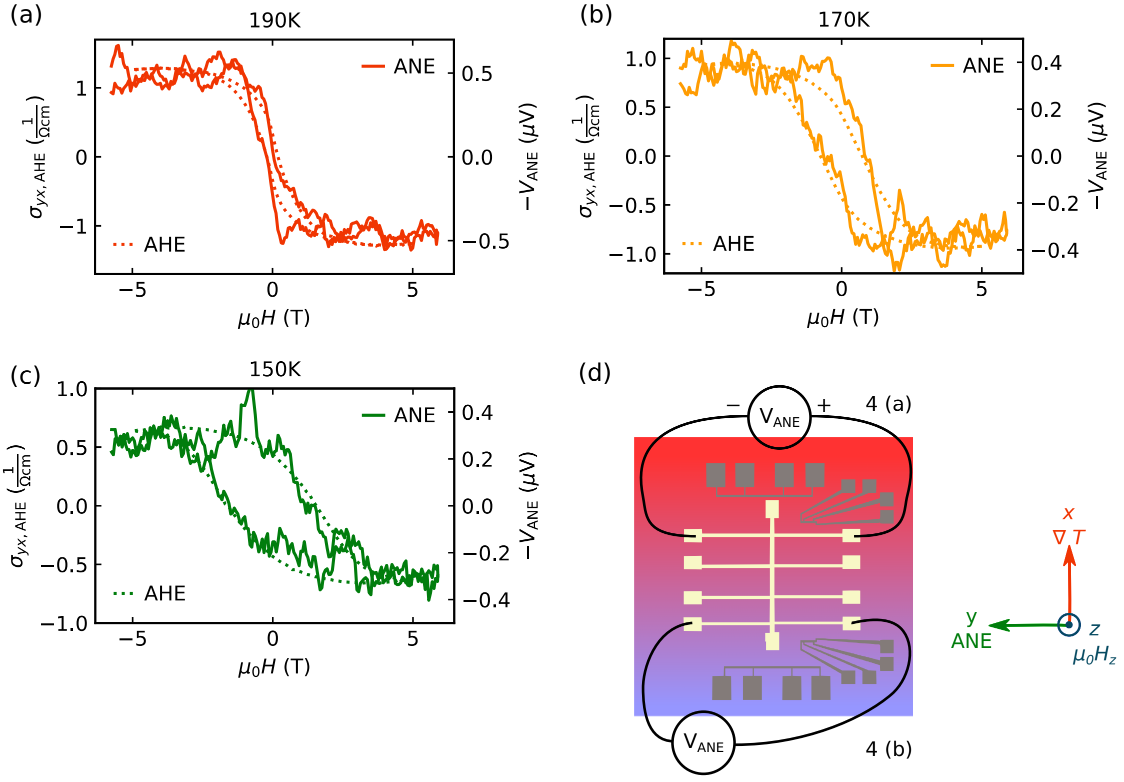

FIG. 3. Comparison of the field dependence of the AHE (dotted curves) and ANE (solid curves) curves. Base temperatures of (a) 190 K, (b) 170 K, and (c) 150 K . (d) Schematic of the sample setup used to measure the anomalous Nernst effect. The upper heater is at $x = 0.963\,\mathrm{mm}$, the upper transversal bar is at $x = 0.5\,\mathrm{mm}$, and the lower transversal bar is at $x = -0.5\,\mathrm{mm}$.

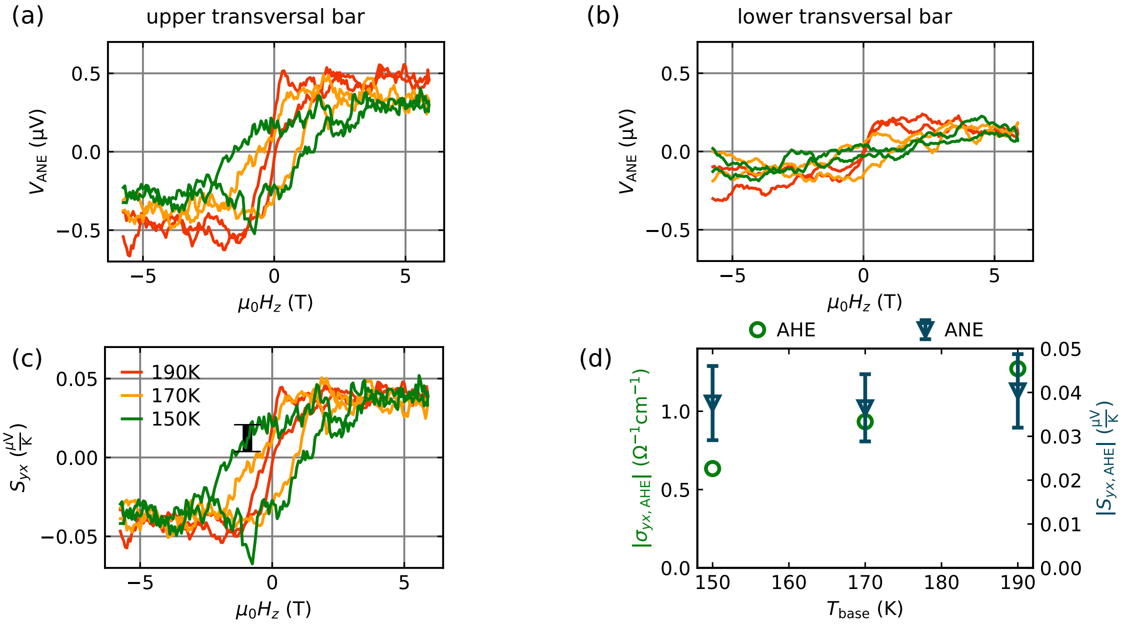

FIG. 4. Measurements of the anomalous Nernst effect. (a) Magnetic-field dependence of the anomalous Nernst voltage on the upper transversal bar ($x = 0.5$ mm) for different temperatures. (b) Magnetic-field dependence of the anomalous Nernst voltage on the lower transversal bar ($x = -0.5$ mm) for different temperatures. (c) Magnetic-field dependence of the ANE on the upper transversal bar for different temperatures, normalized to the mean ANE for each temperature. (d) Comparison of the temperature dependences of the AHE and the ANE.

where V_y is the transversal voltage between the contacts, w_{bond} is the distance between the contacts, and $\nabla_x T_{\mathrm{loc,meas}}$ is the thermal gradient along x, which was corrected for the spatial variation by using the FEM simulation results. The correction was calculated in the following way. We used the simulated local temperature gradients $\nabla_x T_{\mathrm{loc,simu}}(x)$ and global temperature difference $\Delta T_{\mathrm{glob,simu}}$, as well as the measured global temperature difference $\Delta T_{\mathrm{glob,meas}}$, to calculate the local temperature gradients $\nabla_x T_{\mathrm{loc,meas}}$ for each base temperature, heater power, and distance from the heater as

$$\nabla_x T_{\mathrm{loc,meas}} = \nabla_x T_{\mathrm{loc,simu}} \times \frac{\Delta T_{\mathrm{glob,meas}}}{\Delta T_{\mathrm{glob,simu}}}. \tag{4}$$

The inhomogeneity of the temperature along the y direction can also be estimated from the FEM simulation results. We considered this inhomogeneity in calculating the simulated temperature difference $\Delta T_{\mathrm{glob,simu}}$ and temperature gradient $\nabla_x T_{\mathrm{loc,simu}}$ by averaging the temperature and temperature gradient for each transversal bar over the length of the bar (the y direction).

The resulting anomalous Nernst coefficients are shown in Fig. 4(c). In Fig. 4(d), the temperature dependence of the ANE (blue) is compared to that of the AHE (green). The uncertainties of the Nernst coefficients are estimated by considering the variation of the measured values for the different transversal contact pairs as well as the above-mentioned uncertainties of the measured thermal gradient, leading to the error bars depicted in Fig. 4(d) and Table II. The AHE is decreasing within that temperature range, as expected for $\mathrm{Mn_3NiN}$ films grown on STO, as shown by Boldrin *et al.* [25]. The change in the anomalous Nernst coefficient in the investigated temperature range is smaller than its uncertainties. Therefore, we can say only that the change in the ANE is smaller than 20% within the temperature range. The temperature dependences of AHE and ANE can be different and are connected via the Mott relation [33,34,43], but a closer investigation of this temperature dependence in the context of the Mott relation is beyond the scope of this study.

In addition to determining the ANE, we evaluated the Seebeck coefficient S_{xx} by measuring the voltage V_x at the longitudinal bar at the investigated temperatures and the applied temperature gradient. The Seebeck coefficient is defined as [33]

$$S_{xx} = -\frac{V_x}{\Delta T}. \tag{5}$$

As the temperature profile of the sample was also inhomogeneous, we used the FEM simulation results and the measured global temperature difference to calculate the local temperature difference ΔT between the two contacts of the longitudinal bar.

Having determined the anomalous Hall conductivity $\sigma_{yx,\mathrm{AHE}}$, the longitudinal conductivity σ_{xx}, the Seebeck coefficient S_{xx}, and the anomalous Nernst coefficient $S_{yx,\mathrm{ANE}}$, we finally calculated the anomalous Nernst conductivity $\alpha_{yx,\mathrm{ANE}}$ as [34]

$$\alpha_{yx,\mathrm{ANE}} = \sigma_{xx} S_{yx,\mathrm{ANE}} + \sigma_{yx,\mathrm{AHE}} S_{xx}. \tag{6}$$

Note that the longitudinal conductivity σ_{xx}, the Seebeck coefficient S_{xx}, and the Nernst coefficient $S_{yx,\mathrm{ANE}}$ are positive, whereas the anomalous Hall conductivity $\sigma_{yx,\mathrm{AHE}}$ is negative. The anomalous Nernst conductivity $\alpha_{yx,\mathrm{ANE}}$ is then positive because $|\sigma_{xx} S_{yx}| > |\sigma_{yx} S_{xx}|$. The transport coefficients used to calculate the anomalous Nernst conductivity α_{yx} are shown in Table II. As described by Boldrin *et al.*, $\mathrm{Mn_3NiN}$ films grown on STO show a ferrimagnetic phase above their Néel

TABLE II. Transport coefficients used to calculate the Nernst conductivity $\alpha_{yx,\mathrm{ANE}}$.

T (K)	σ_{xx} (Ω^{-1} cm^{-1})	$\sigma_{yx,\mathrm{AHE}}$ (Ω^{-1} cm^{-1})	S_{xx} (µV/K)	$S_{yx,\mathrm{ANE}}$ (µV/K)	$\alpha_{yx,\mathrm{ANE}}$ A/(K m)
190	974.93	−1.272	1.70	0.0404(84)	0.00372(82)
170	964.76	−0.933	2.39	0.0365(77)	0.00330(74)
150	956.91	−0.634	2.94	0.0376(85)	0.00341(81)

temperature. The values of the measured transport coefficients in the ferrimagnetic phase can be found in Sec. S2 of the Supplemental Material [32] (see also Ref. [44] therein).

The measured ANE conductivity of $\alpha_{yx} = 0.00348$ A/(Km) (the average of the measurements in the temperature range from 150 to 190 K) is significantly smaller than the theoretically predicted $|\alpha_{yx}| = 1.80$ A/(Km) [7]. There are multiple possible reasons for this difference that are discussed below. Note that only the projection of the Hall vector onto the out-of-plane (e.g., [001]) direction was experimentally measured, whereas the theoretical value corresponds to the [111] direction. However, projecting the [111] direction on the [001] direction in a cubic crystal would lead to only a factor of $\frac{1}{\sqrt{3}}$, which would not explain the observed discrepancy of two orders of magnitude.

Another possible reason for the discrepancy between the experimental and theoretical results could be the multidomain character of the sample. Both Γ^{4g} and Γ^{5g} phases can coexist [7] in Mn_3NiN. The Γ^{4g} phase alone can break into eight equivalent domains. The Hall vectors and net moments corresponding to the eight domains were summarized by Johnson *et al.* [13]. The overall Nernst effect could thus be reduced due to the multidomain character of the sample. However, the domain population in an antiferromagnet can be controlled by cooling the material under a magnetic field from above the Néel temperature [11,13]. To investigate the effect of the domain structure on our ANE signal, we cooled the sample in various magnetic field orientations and in zero field from above the Néel temperature (e.g., 300 K) down to 190 K. We did not observe any variation of the measured ANE signal, as demonstrated by Fig. 5. This result suggests that the multidomain character of the sample cannot account for the small ANE coefficient. Another possible reason for the discrepancy between the theoretical and experimental results is the strong sensitivity of the anomalous Nernst effect to the position of the Fermi level. The ANE is dominated by the Berry curvature at the Fermi level, unlike the AHE, which has contributions from all the occupied energy bands. As shown by Zhou *et al.* [7] in Fig. 3(c), the anomalous Nernst conductivity can be reduced, can be eliminated, or can even change sign if the Fermi level is shifted by only 30 meV. The position of the Fermi level is experimentally very sensitive to the stoichiometry and purity of a particular sample. The calculations also do not include scattering, which can play a significant role in a real sample and to which the ANE may be particularly sensitive. Assuming a single-band model, one could calculate the charge carrier densities to be between 3.25×10^{21} and 4.73×10^{21} $^1/_{cm^3}$ for temperatures between 150 and 190 K from the linear contributions to the Hall effect. This values would be consistent with the charge carrier density of 2.4×10^{21} $^1/_{cm^3}$ calculated by Boldrin *et al.* [25] using DFT calculations at zero temperature. However, in the case of Mn_3NiN a single-band model cannot be used due to the complex band structure. Furthermore, it cannot be guaranteed that there are no other linear contributions to the Hall effect at high fields, so we hesitate to deduce any information from the ordinary Hall coefficient with regard to charge carrier density.

Similarly, the strain induced by the substrate can strongly influence the position of the Fermi level; consequently, the ANE becomes a sensitive probe of the strain-induced changes, as You *et al.* [30] illustrated. The calculation results presented in Fig. 2(b) of a study by Boldrin *et al.* [18] show that strain can influence the energy dependence of the anomalous Hall conductivity and therefore also the ANE.

Clearly, there are several possible explanations for the discrepancy between the experimental and theoretical values of the anomalous Nernst conductivity, warranting further study. Nevertheless, Mn_3NiN offers an ideal platform to explore the spin-caloritronic phenomena because the ANE can be measured both by the in- and out-of-plane thermal gradients in one device simultaneously [45]. This is because the noncollinear magnetic structure causes all the off-diagonal elements of the Hall conductivity to be nonzero; that is, as the Hall vector is close to the body diagonal, both thermal gradients can

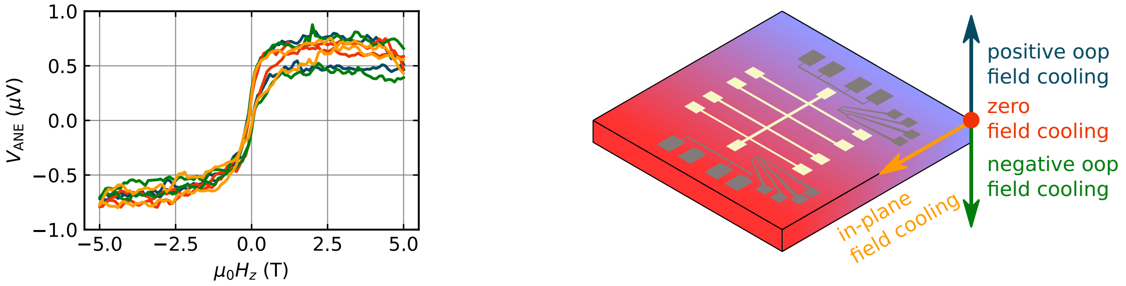

FIG. 5. Anomalous Nernst voltages at $T_{\mathrm{base}} = 190$ K for different field-cooling orientations and without field cooling. Field cooling was performed by cooling the sample from 300 to 190 K in a field of 5 T with different orientations (blue, yellow, and green curves) and with no field (red curve).

generate transverse voltage. Moreover, the out-of-plane thermal gradient can be applied either locally [13] or globally [30].

V. SUMMARY AND OUTLOOK

In conclusion, we measured the anomalous Hall and Nernst effects in Mn_3NiN in the same sample. We used our experimental data and finite-element simulation results to obtain the anomalous Nernst coefficient in the Mn_3NiN thin film as $0.0382\,^{\mu V}/_{K}$. The anomalous Nernst conductivity was measured as $\alpha_{yx} = 0.00348\,\mathrm{A/(Km)}$ (by averaging the respective values over the temperature range from 150 to 190 K), which is significantly smaller than the theoretical prediction of $|\alpha_{yx}| = 1.8\,\mathrm{A/(Km)}$. To accurately determine the ANE coefficient, we paid special attention to characterizing the spatial distribution of the thermal gradient in our sample, and we supported our measurements by FEM simulations. A likely reason for the discrepancy between the experimental and theoretical ANE values is the particular position of the Fermi level in our samples. We propose Mn_3NiN films with a [001] film normal as a fundamentally interesting model system to explore the rich physics of noncollinear antiferromagnets. In addition, a Mn_3NiN film is a good model system for simultaneous in-plane and out-of-plane thermal gradient measurements to explore the anisotropy of the ANE in this class of materials.

ACKNOWLEDGMENTS

S.B. was supported by the DFG through Project No. C08 of SFB 1143. This study was supported in part by the Ministry of Education of the Czech Republic Grant No. LM2018110 and LNSM-LNSpin and by the Czech Science Foundation (Grant No. 22-17899K). D.K. acknowledges Lumina Quaeruntur Fellowship No. LQ100102201 of the Czech Academy of Science. J.Ž. was supported by the Ministry of Education, Youth and Sports of the Czech Republic from the OP RDE program under the project International Mobility of Researchers MSCAIF at CTU (No. CZ.02.2.69/0.0/0.0/18 070/0010457) and through the e-INFRA CZ (ID. No. 90254). E.S. and P.N. would like to acknowledge the Czech Science Foundation (Grant No. 19-28375X). S.T.B.G., A.T., and H.R. were funded by the Deutsche Forschungsgemeinschaft (DFG, German Research Foundation), Grant No. 490730630. S.T.B.G. was funded by the Deutsche Forschungsgemeinschaft (DFG, German Research Foundation), Grant No. 445976410.

---

[1] L. Ding, J. Koo, L. Xu, X. Li, X. Lu, L. Zhao, Q. Wang, Q. Yin, H. Lei, B. Yan, Z. Zhu, and K. Behnia, Intrinsic Anomalous Nernst Effect Amplified by Disorder in a Half-Metallic Semimetal, Phys. Rev. X **9**, 041061 (2019).

[2] H. Chen, Q. Niu, and A. H. MacDonald, Anomalous Hall Effect Arising from Noncollinear Antiferromagnetism, Phys. Rev. Lett. **112**, 017205 (2014).

[3] M. Ikhlas, T. Tomita, T. Koretsune, M.-T. Suzuki, D. Nishio-Hamane, R. Arita, Y. Otani, and S. Nakatsuji, Large anomalous Nernst effect at room temperature in a chiral antiferromagnet, Nat. Phys. **13**, 1085 (2017).

[4] T. Chen, S. Minami, A. Sakai, Y. Wang, Z. Feng, T. Nomoto, M. Hirayama, R. Ishii, T. Koretsune, R. Arita, and S. Nakatsuji, Large anomalous Nernst effect and nodal plane in an iron-based kagome ferromagnet, Sci. Adv. **8**, eabk1480 (2022).

[5] T. Asaba, V. Ivanov, S. M. Thomas, S. Y. Savrasov, J. D. Thompson, E. D. Bauer, and F. Ronning, Colossal anomalous Nernst effect in a correlated noncentrosymmetric kagome ferromagnet, Sci. Adv. **7**, eabf1467 (2021).

[6] Y. Pan, C. Le, B. He, S. J. Watzman, M. Yao, J. Gooth, J. P. Heremans, Y. Sun, and C. Felser, Giant anomalous Nernst signal in the antiferromagnet $YbMnBi_2$, Nat. Mater. **21**, 203 (2022).

[7] X. Zhou, J.-P. Hanke, W. Feng, S. Blügel, Y. Mokrousov, and Y. Yao, Giant anomalous Nernst effect in noncollinear antiferromagnetic Mn-based antiperovskite nitrides, Phys. Rev. Mater. **4**, 024408 (2020).

[8] C. Wuttke, F. Caglieris, S. Sykora, F. Scaravaggi, A. U. B. Wolter, K. Manna, V. Süss, C. Shekhar, C. Felser, B. Büchner, and C. Hess, Berry curvature unravelled by the anomalous Nernst effect in Mn_3Ge, Phys. Rev. B **100**, 085111 (2019).

[9] J. Noky, J. Gooth, C. Felser, and Y. Sun, Characterization of topological band structures away from the Fermi level by the anomalous Nernst effect, Phys. Rev. B **98**, 241106(R) (2018).

[10] J. Z. Sun, W. J. Gallagher, P. R. Duncombe, L. Krusin-Elbaum, R. A. Altman, A. Gupta, Y. Lu, G. Q. Gong, and G. Xiao, Observation of large low-field magnetoresistance in trilayer perpendicular transport devices made using doped manganate perovskites, Appl. Phys. Lett. **69**, 3266 (1996).

[11] H. Reichlova, T. Janda, J. Godinho, A. Markou, D. Kriegner, R. Schlitz, J. Zelezny, Z. Soban, M. Bejarano, H. Schultheiss, P. Nemec, T. Jungwirth, C. Felser, J. Wunderlich, and S. T. B. Goennenwein, Imaging and writing magnetic domains in the non-collinear antiferromagnet Mn_3Sn, Nat. Commun. **10**, 5459 (2019).

[12] T. Janda *et al.*, Magneto-Seebeck microscopy of domain switching in collinear antiferromagnet CuMnAs, Phys. Rev. Mater. **4**, 094413 (2020).

[13] F. Johnson, J. Kimák, J. Zemen, Z. Šobáň, E. Schmoranzerová, J. Godinho, P. Němec, S. Beckert, H. Reichlová, D. Boldrin, J. Wunderlich, and L. F. Cohen, Identifying the octupole antiferromagnetic domain orientation in Mn_3NiN by scanning anomalous Nernst effect microscopy, Appl. Phys. Lett. **120**, 232402 (2022).

[14] W. Zhou and Y. Sakuraba, Heat flux sensing by anomalous Nernst effect in Fe-Al thin films on a flexible substrate, Appl. Phys. Express **13**, 043001 (2020).

[15] T. Nan *et al.*, Controlling spin current polarization through non-collinear antiferromagnetism, Nat. Commun. **11**, 4671 (2020).

[16] G. Gurung, D.-F. Shao, and E. Y. Tsymbal, Spin-torque switching of noncollinear antiferromagnetic antiperovskites, Phys. Rev. B **101**, 140405(R) (2020).

[17] L. Flórez-Gómez, W. Ibarra-Hernández, and A. C. Garcia-Castro, Lattice dynamics and spinphonon coupling in the noncollinear antiferromagnetic antiperovskite Mn_3NiN, J. Magn. Magn. Mater. **562**, 169813 (2022).

[18] D. Boldrin, I. Samathrakis, J. Zemen, A. Mihai, B. Zou, F. Johnson, B. D. Esser, D. W. McComb, P. K. Petrov, H. Zhang,

and L. F. Cohen, Anomalous Hall effect in noncollinear antiferromagnetic $\mathrm{Mn_3NiN}$ thin films, Phys. Rev. Mater. **3**, 094409 (2019).

[19] Y. You, H. Bai, X. Chen, Y. Zhou, X. Zhou, F. Pan, and C. Song, Room temperature anomalous Hall effect in antiferromagnetic $\mathrm{Mn_3SnN}$ films, Appl. Phys. Lett. **117**, 222404 (2020).

[20] T. Hajiri, S. Ishino, K. Matsuura, and H. Asano, Electrical current switching of the noncollinear antiferromagnet $\mathrm{Mn_3GaN}$, Appl. Phys. Lett. **115**, 052403 (2019).

[21] B. H. Rimmler, B. K. Hazra, B. Pal, K. Mohseni, J. M. Taylor, A. Bedoya-Pinto, H. Deniz, M. Tangi, I. Kostanovskiy, C. Luo, R. R. Neumann, A. Ernst, F. Radu, I. Mertig, H. L. Meyerheim, and S. S. P. Parkin, Atomic displacements enabling the observation of the anomalous Hall effect in a non-collinear antiferromagnet, Adv. Mater. **35**, 2209616 (2023).

[22] A. Rajan, T. G. Saunderson, F. R. Lux, R. Y. Díaz, H. M. Abdullah, A. Bose, B. Bednarz, J.-Y. Kim, D. Go, T. Hajiri, G. Shukla, O. Gomonay, Y. Yao, W. Feng, H. Sasno, U. Schwingenschlögl, L. López-Díaz, J. Sinova, Y. Mokrousov, A. Manchon, and M. Kläui, Revealing the higher-order spin nature of the Hall effect in non-collinear antiferromagnet $\mathrm{Mn_3Ni_{0.35}Cu_{0.65}N}$, arXiv:2304.10747.

[23] X. Zhou, J.-P. Hanke, W. Feng, F. Li, G.-Y. Guo, Y. Yao, S. Blügel, and Y. Mokrousov, Spin-order dependent anomalous Hall effect and magneto-optical effect in the noncollinear antiferromagnets $\mathrm{Mn_3}X\mathrm{N}$ with $X = \mathrm{Ga}$, Zn, Ag, or Ni, Phys. Rev. B **99**, 104428 (2019).

[24] H. K. Singh, I. Samathrakis, N. M. Fortunato, J. Zemen, C. Shen, O. Gutfleisch, and H. Zhang, Multifunctional antiperovskites driven by strong magnetostructural coupling, npj Comput. Mater. **7**, 98 (2021).

[25] D. Boldrin, F. Johnson, R. Thompson, A. P. Mihai, B. Zou, J. Zemen, J. Griffiths, P. Gubeljak, K. L. Ormandy, P. Manuel, D. D. Khalyavin, B. Ouladdiaf, N. Qureshi, P. Petrov, W. Branford, and L. F. Cohen, The biaxial strain dependence of magnetic order in spin frustrated $\mathrm{Mn_3NiN}$ thin films, Adv. Funct. Mater. **29**, 1902502 (2019).

[26] D. Boldrin, A. P. Mihai, B. Zou, J. Zemen, R. Thompson, E. Ware, B. V. Neamtu, L. Ghivelder, B. Esser, D. W. McComb, P. Petrov, and L. F. Cohen, Giant piezomagnetism in $\mathrm{Mn_3NiN}$, ACS Appl. Mater. Interfaces **10**, 18863 (2018).

[27] J. Zemen, Z. Gercsi, and K. G. Sandeman, Piezomagnetism as a counterpart of the magnetovolume effect in magnetically frustrated Mn-based antiperovskite nitrides, Phys. Rev. B **96**, 024451 (2017).

[28] F. Johnson, D. Boldrin, J. Zemen, D. Pesquera, J. Kim, X. Moya, H. Zhang, H. K. Singh, I. Samathrakis, and L. F. Cohen, Strain dependence of Berry-phase-induced anomalous Hall effect in the non-collinear antiferromagnet $\mathrm{Mn_3NiN}$, Appl. Phys. Lett. **119**, 222401 (2021).

[29] M. Ikhlas, S. Dasgupta, F. Theuss, T. Higo, S. Kittaka, B. J. Ramshaw, C. W. Hicks, and S. Nakatsuji, Piezomagnetic switching of the anomalous Hall effect in an antiferromagnet at room temperature, Nat. Phys. **18**, 1086 (2022).

[30] Y. You, H. Lam, C. Wan, C. Wan, W. Zhu, L. Han, H. Bai, Y. Zhou, L. Qiao, T. Chen, F. Pan, J. Liu, and C. Song, Anomalous Nernst Effect in an Antiperovskite Antiferromagnet, Phys. Rev. Appl. **18**, 024007 (2022).

[31] COMSOL AB, COMSOL MULTIPHYSICS, version 6.0, https://www.comsol.com.

[32] See Supplement Material at http://link.aps.org/supplemental/10.1103/PhysRevB.108.024420 for the anomalous Hall conductivity depending on the longitudinal conductivity for different materials, including our investigated film, as well as the transport coefficients above the Néel temperature and a description of the evaluation of the intrinsic magnetization of the thin film.

[33] G.-H. Park, H. Reichlova, R. Schlitz, M. Lammel, A. Markou, P. Swekis, P. Ritzinger, D. Kriegner, J. Noky, J. Gayles, Y. Sun, C. Felser, K. Nielsch, S. T. B. Goennenwein, and A. Thomas, Thickness dependence of the anomalous Nernst effect and the Mott relation of Weyl semimetal $\mathrm{Co_2MnGa}$ thin films, Phys. Rev. B **101**, 060406(R) (2020).

[34] Y. Pu, D. Chiba, F. Matsukura, H. Ohno, and J. Shi, Mott Relation for Anomalous Hall and Nernst Effects in $\mathrm{Ga}_{1-x}\mathrm{Mn}_x\mathrm{As}$ Ferromagnetic Semiconductors, Phys. Rev. Lett. **101**, 117208 (2008).

[35] D. Boldrin, I. Samathrakis, J. Zemen, A. Mihai, B. Zou, F. Johnson, B. D. Esser, D. W. McComb, P. K. Petrov, H. Zhang, and L. F. Cohen, Anomalous Hall effect in noncollinear antiferromagnetic $\mathrm{Mn_3NiN}$ thin films, arXiv:1902.04357v1 (2019).

[36] L. Smrcka and P. Streda, Transport coefficients in strong magnetic fields, J. Phys. C **10**, 2153 (1977).

[37] N. Nagaosa, J. Sinova, S. Onoda, A. H. MacDonald, and N. P. Ong, Anomalous Hall effect, Rev. Mod. Phys. **82**, 1539 (2010).

[38] T. C. Chuang, P. L. Su, P. H. Wu, and S. Y. Huang, Enhancement of the anomalous Nernst effect in ferromagnetic thin films, Phys. Rev. B **96**, 174406 (2017).

[39] A. Markou, D. Kriegner, J. Gayles, L. Zhang, Y.-C. Chen, B. Ernst, Y.-H. Lai, W. Schnelle, Y.-H. Chu, Y. Sun, and C. Felser, Thickness dependence of the anomalous Hall effect in thin films of the topological semimetal $\mathrm{Co_2MnGa}$, Phys. Rev. B **100**, 054422 (2019).

[40] Y. M. Lu, J. W. Cai, Z. Guo, and X. X. Zhang, Unconventional scaling of the anomalous Hall effect accompanying electron localization correction in the dirty regime, Phys. Rev. B **87**, 094405 (2013).

[41] A. Oiwa, A. Endo, S. Katsumoto, Y. Iye, H. Ohno, and H. Munekata, Magnetic and transport properties of the ferromagnetic semiconductor heterostructures (In,Mn)As/(Ga,Al)Sb, Phys. Rev. B **59**, 5826 (1999).

[42] A. M. Dehkordi, S. Bhattacharya, T. Darroudi, M. Karakaya, C. Kucera, J. Ballato, R. Adebisi, J. R. Gladden, R. Podila, A. M. Rao, H. N. Alshareef, and T. M. Tritt, Optimizing thermal conduction in bulk polycrystalline $\mathrm{SrTiO_{3-\delta}}$ ceramics via oxygen non-stoichiometry, MRS Commun. **8**, 1470 (2018).

[43] K. Geishendorf, P. Vir, C. Shekhar, C. Felser, J. I. Facio, J. van den Brink, K. Nielsch, A. Thomas, and S. Goennenwein, Signatures of the magnetic entropy in the thermopower signals in nanoribbons of the magnetic Weyl semimetal $\mathrm{Co_3Sn_2S_2}$, Nano Lett. **20**, 300 (2020).

[44] F. Johnson, J. Zazvorka, L. Beran, D. Boldrin, L. F. Cohen, J. Zemen, and M. Veis, Room-temperature weak collinear ferrimagnet with symmetry-driven large intrinsic magneto-optic signatures, Phys. Rev. B **107**, 014404 (2023).

[45] M. Schreier, N. Roschewsky, E. Dobler, S. Meyer, H. Huebl, R. Gross, and S. T. B. Goennenwein, Current heating induced spin Seebeck effect, Appl. Phys. Lett. **103**, 242404 (2013).